

Observationally derived magnetic field strength and 3D components in the HD 142527 disk

Received: 22 April 2024

Accepted: 28 November 2024

Published online: 05 February 2025

 Check for updates

Satoshi Ohashi^{1,2}✉, Takayuki Muto³, Yusuke Tsukamoto⁴, Akimasa Kataoka^{1,5}, Takashi Tsukagoshi⁶, Munetake Momose⁷, Misato Fukagawa¹ & Nami Sakai²

The magnetic fields in protoplanetary disks around young stars play an important role in disk evolution and planet formation. Measuring the polarized thermal emission from magnetically aligned grains is a reliable method for tracing magnetic fields. However, it has been difficult to observe magnetic fields from dust polarization in protoplanetary disks because other polarization mechanisms involving grown dust grains become efficient. Here we report multi-wavelength (0.87, 1.3, 2.1 and 2.7 mm) observations of polarized thermal emission in the protoplanetary disk around HD 142527, which shows a lopsided dust distribution. We revealed that smaller dust particles still exhibit magnetic alignment in the southern part of the disk. Furthermore, angular offsets between the observed magnetic field and the disk azimuthal direction were discovered. These offsets can be used to measure the relative strengths of each component of a three-dimensional magnetic field (radial (B_r), azimuthal (B_ϕ) and vertical (B_z)). Applying this method, we derived the magnetic field around a 200 au radius from the protostar as $|B_r|:|B_\phi|:|B_z| \approx 0.26:1:0.23$ with a strength of ~ 0.3 mG. Our observations provide some key parameters of magnetic activities, including the plasma beta, which has had to be assumed in theoretical studies. In addition, the radial and vertical angular momentum transfers were found to be comparable, which poses a challenge to theoretical studies of protoplanetary disks.

HD 142527 is a Herbig Fe star¹ with a mass and age of $\sim 2.4 M_\odot$ and ~ 3 Myr, respectively^{2–4}, and it is 157 pc away from our Solar System^{5,6}. The accretion rate to the star has been estimated to be $10^{-7} M_\odot \text{ yr}^{-1}$ (ref. 7). The disk surrounding the young star exhibits a wide gap with a radial width of about 100 au and a horseshoe-shaped ring structure^{8,9}. The high-contrast emission from its north side is brighter than from its south side, which suggests that there are large dust grains in the northern region and small dust grains in the southern region^{10,11}. Therefore, the protoplanetary disk around HD 142527 is an ideal laboratory for

investigating grain growth, which is considered to be the first step in planet formation. We analysed the polarization data of the dust continuum emission at wavelengths of 0.87 mm (band 7), 1.3 mm (band 6), 2.1 mm (band 4) and 2.7 mm (band 3) obtained by the Atacama Large Millimeter/submillimeter Array (ALMA) (Methods).

Results

Figure 1 shows images of Stokes I , polarized intensity (PI) and polarization fraction (PF) at these wavelengths. The polarization vectors (PA)

A full list of affiliations appears at the end of the paper. ✉ e-mail: satoshi.ohashi@nao.ac.jp

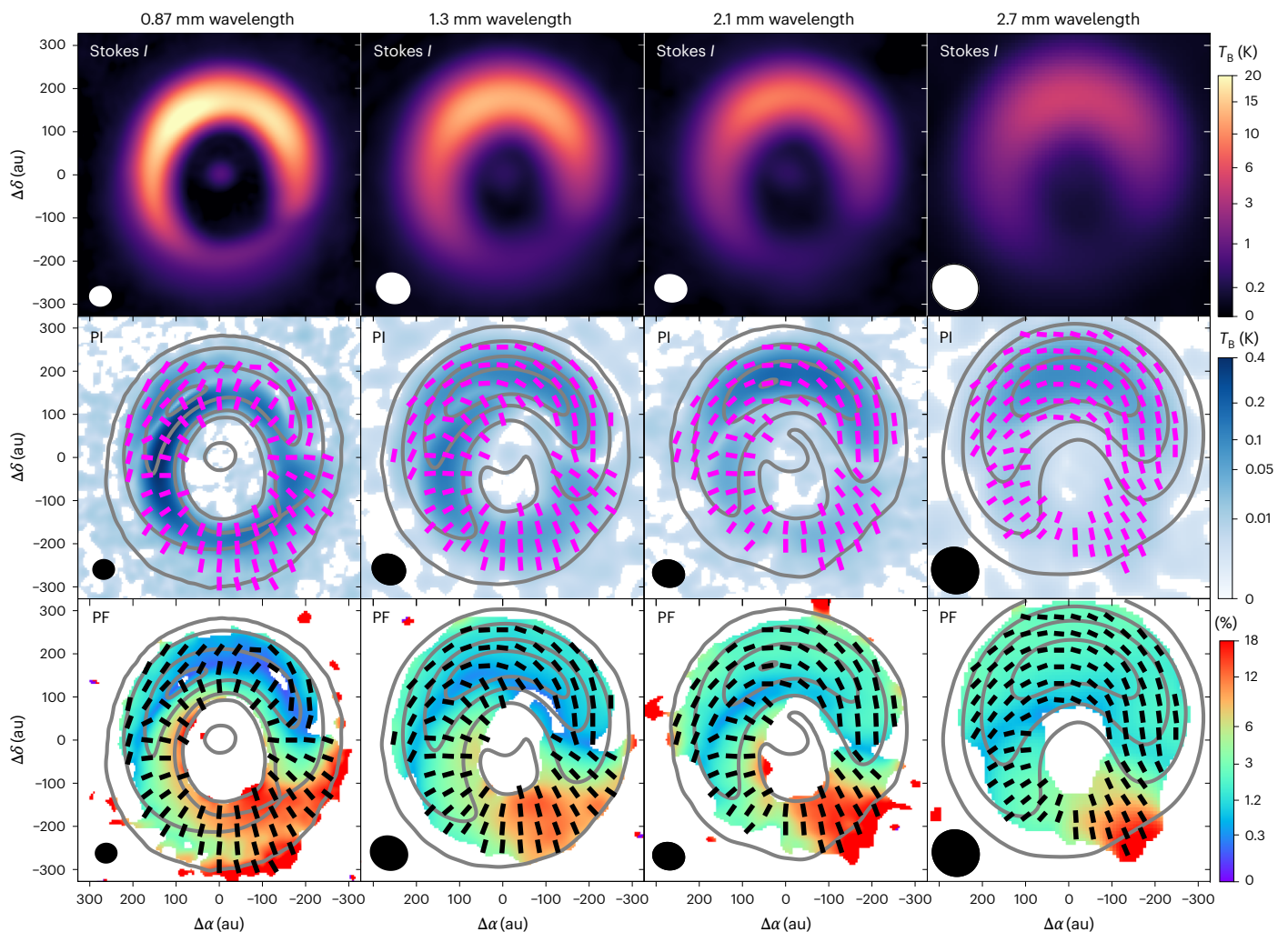


Fig. 1 | Polarized thermal emission from dust grains in the protoplanetary disk around HD 142527. Stokes I (top), polarized intensity (PI) (middle) and polarization fraction (PF) (bottom) at 0.87, 1.3, 2.1 and 2.7 mm wavelengths plotted against right ascension ($\Delta\alpha$) and declination ($\Delta\delta$). Polarization vectors are also shown on the PI and PF images. The Stokes I and PI are converted to the brightness temperature (T_B) by assuming the Rayleigh–Jeans approximation.

The PF and polarization vectors are plotted where the polarized intensity is detected above the 3σ noise level. Contours on the PI and PF images indicate the brightness temperatures of the Stokes I emission of [0.1, 1, 10, 20] K for 0.87 mm, [0.1, 1, 5, 10, 20] K for 1.3 mm, [0.1, 1, 5, 9] K for 2.1 mm and [0.06, 0.3, 1, 3] K for 2.7 mm. The resolution (beam size) is shown as a small ellipse in the lower left corner of each panel.

are also plotted on the PI and PF images. The horseshoe structure can be recognized in the Stokes I images at all wavelengths, as revealed in previous observations^{8–11}. Although the Stokes I images are similar in these wavelengths, the polarization images show different morphologies. In particular, the polarization vectors and fraction in the northern region change significantly with wavelength. The 0.87 mm polarization vectors show a flip around the peak of the Stokes I emission, as also shown in previous studies^{10,12}, whereas the 2.1 and 2.7 mm polarization vectors seem to be almost azimuthally aligned. The 1.3 mm polarization vectors also show the flip, although it is less prominent¹³. These different polarization patterns can be explained by the contribution of the self-scattering, which is efficient only when the maximum grain size is close to the observing wavelength. Therefore, dust grains of size $\sim 100\ \mu\text{m}$ are abundant in the northern region^{12,14}. In contrast to the northern region, the southern region shows almost the same polarization pattern regardless of the observed wavelength. All the polarization vectors are in the radial direction, and the polarization fraction reaches as high as 15%.

The consistent polarization vectors and polarization fractions in the southern region (position angle of 100° – 250° ; Methods and Supplementary Figs. 1, 2 and 3) suggest that the polarization is produced by grain alignment rather than self-scattering. The high polarization

($\sim 15\%$) in the radial direction is expected to originate from the magnetically aligned grains^{15,16} under the toroidal magnetic field^{17–19}. By contrast, other alignment mechanisms, such as radiative alignment or mechanical alignment, predict azimuthally polarized emission^{20–22}, which may be the case for the 1.3, 2.1 and 2.7 mm polarizations in the northern region. Note that the magnetic alignment also predicts azimuthally polarized emission at millimetre wavelengths when the dust is larger than 1 mm due to the negative polarization fraction in the Mie regime²³. Therefore, we conclude that at least the smaller dust grains in the southern region are magnetically aligned, as occurs in the interstellar medium^{15,16}. This may imply that the dust grains in the southern region contain large iron inclusions that are aligned with the magnetic field in the protoplanetary disks²⁴.

For the southern region, the polarization vector is expected to be perpendicular to the magnetic field direction projected onto the sky plane. Thus, we investigated the magnetic morphology by rotating the polarization vectors by 90° . Figure 2 indicates that the toroidal field is dominant, as expected from magnetohydrodynamics simulations^{25–27}. To further constrain the magnetic field structure, we measured the angular offset of the observed magnetic field from the purely toroidal case, assuming a disk inclination and position angle of 27° and 161° , respectively^{6,28}.

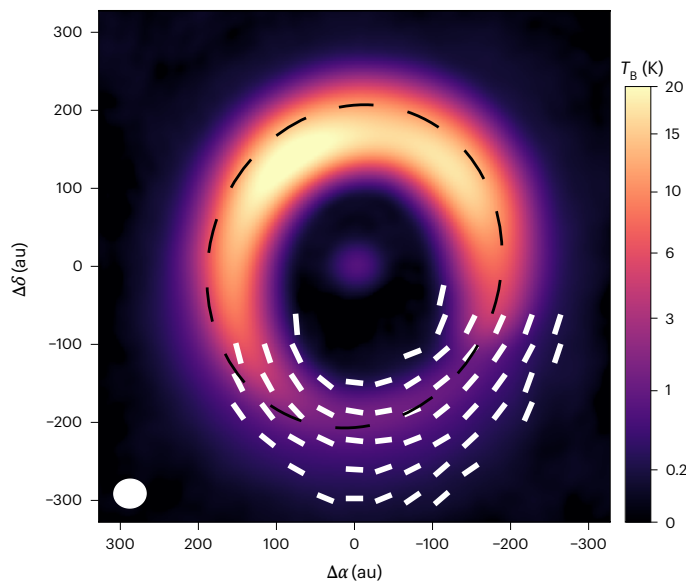


Fig. 2 | Magnetic field morphology of the HD 142527 disk. The magnetic field is shown by the white segments superimposed on the 0.87 mm Stokes / continuum image, which was derived by rotating the 0.87 mm polarization vectors by 90° because the dust polarization is caused by the thermal emission of magnetically aligned dust grains in the southern region. The black dashed line indicates the azimuthal direction of the disk and has a radius of 210 au.

Three-dimensional magnetic field

Figure 3 shows the angular difference ($\Delta\phi = B_\phi - B_{\text{obs}}$) between the observed magnetic field (B_{obs}) and the pure toroidal magnetic field (B_ϕ) as a function of position angle at 200 ± 50 au from the central star in the southern region. From this figure, we found that the observed magnetic field has systemic offsets of about 10° from the toroidal case. We interpret these offsets as being caused by the radial and vertical components of the magnetic fields in the disk.

Single-layer model

Here we propose a method for estimating the relative strengths of the three-dimensional components of the magnetic fields: radial (B_r), azimuthal (B_ϕ) and vertical (B_z). The B_r and B_z components act to deviate the sky-projected magnetic field vector from the purely toroidal direction. Their effects vary at different locations on the disk (Fig. 4), causing azimuthal variations in the angular offsets, even if the intrinsic magnetic field exerted on the disk is homogeneous. The angular offset was estimated with

$$\Delta\phi = \arctan \left\{ \frac{(B_r)_{\phi\perp} + (B_{z,\text{proj}})_{\phi\perp}}{B_\phi + (B_r)_\phi + (B_{z,\text{proj}})_\phi} \right\}, \quad (1)$$

where $(B_r)_{\phi\perp}$ is the component perpendicular to the azimuthal direction in sky-projected B_r , $(B_r)_\phi$ is the component parallel to the azimuthal direction in sky-projected B_r , $B_{z,\text{proj}} = B_z \sin(\text{inclination})$ is the sky-projected strength, $(B_{z,\text{proj}})_{\phi\perp}$ is the component perpendicular to the azimuthal direction in $B_{z,\text{proj}}$ and $(B_{z,\text{proj}})_\phi$ is the component parallel to the azimuthal direction in $B_{z,\text{proj}}$. These parameters are functions of the position angle, as can be seen by considering the projected direction of the grain alignment in the inclined disk geometry. Thus, the variation of the offset value $\Delta\phi$ with position angle allowed us to estimate the relative strengths of the three-dimensional magnetic field. We found that $|B_r|:|B_\phi|:|B_z| = 0.26:1:0.23$ from the chi-squared test best fitted the observations, as shown in Fig. 3. The reduced chi-square value for the best-fitting model is approximately 9, suggesting that more detailed observations and refined models are necessary for giving a better

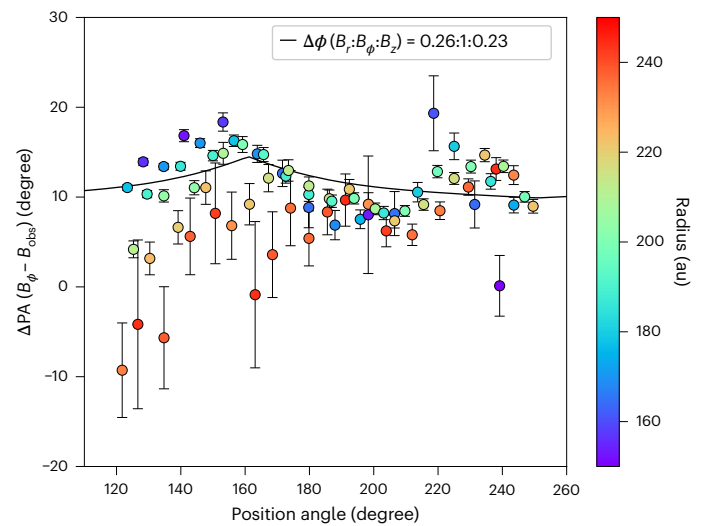


Fig. 3 | Angular difference between the observed magnetic field and the toroidal magnetic field as a function of position angle. Angular difference ($\Delta\phi = B_\phi - B_{\text{obs}}$) between the observed magnetic field (B_{obs}) and the pure toroidal magnetic field (B_ϕ) as a function of position angle at 200 ± 50 au from the central star in the southern region. The colour indicates the radius from the central star. The data were obtained using Nyquist sampling (half of the beam size) with a disk radius of 200 ± 50 au. The data are presented as the median of the distribution with the errors corresponding to the 68th percentiles. There is a systemic offset of about 10°, which was caused by the contributions of the radial (B_r) and vertical (B_z) magnetic fields. The black line shows the best-fitting parameter $|B_r|:|B_\phi|:|B_z| = 0.26:1:0.23$ that explains this offset. Note that the fitting errors are not shown because they are not meaningful due to the large, reduced chi-square value of approximately 9 for the best-fitting model.

understanding of the fine magnetic structure, such as the radial distribution. Nevertheless, overall, the absolute values and variation of $\Delta\phi$ suggest that the azimuthal (toroidal) magnetic field is dominant, whereas the radial and vertical magnetic field strengths are almost comparable. Note that there is uncertainty in the magnetic field direction because the polarization vectors indicate only the alignment direction. Therefore, we used the absolute values for the relative strength.

We assessed the dependence of the relative strengths $|B_r|:|B_\phi|:|B_z|$ on the angular offsets ($\Delta\phi$) by changing these parameters to confirm the robustness of the best-fitting results. Figure 5 shows four different cases for the relative strengths of the magnetic field. The black line indicates the best-fitting ratio, and the dashed coloured lines are for relative strengths $|B_r|:|B_\phi|:|B_z| = 0.3:1:0.1$ (red), $0.25:1:0.5$ (blue) and $0.2:1:0.3$ (green). As shown in this figure, the systemic offset of $\Delta\phi$ is sensitive to B_r , whereas the variation of $\Delta\phi$ with position angle is sensitive to B_z . Therefore, the absolute values of $\Delta\phi$ and its dependence on the position angle allowed us to derive the relative strengths of B_r , B_ϕ and B_z . By comparing these different parameters, we suggest that the best-fitting ratio $|B_r|:|B_\phi|:|B_z| = 0.26:1:0.23$ is a reasonable estimate.

Dual-layer model

It could be expected that B_ϕ and B_r are probably in opposite directions with respect to the disk midplane due to the entrainment of the initial B_z field by the disk rotation (Extended Data Fig. 1). Thus, the observed offset may be due to a combination of an upper disk layer ($\Delta\phi_+$) and a lower disk layer ($\Delta\phi_-$) (dual-layer model). By considering this effect, we fitted the offset values as a function of the position angle (Methods). The best fit resulted in $|B_r|:|B_\phi|:|B_z| = 0.21:1:0.1$, as shown by the black line in Fig. 6. The reduced chi-square value for the best-fitting model is approximately 16, which is larger than that of the single-layer model. This is because the variation of $\Delta\phi$ (a combination of $\Delta\phi_+$ and $\Delta\phi_-$; equation (2)) with position angle cannot be reproduced by the

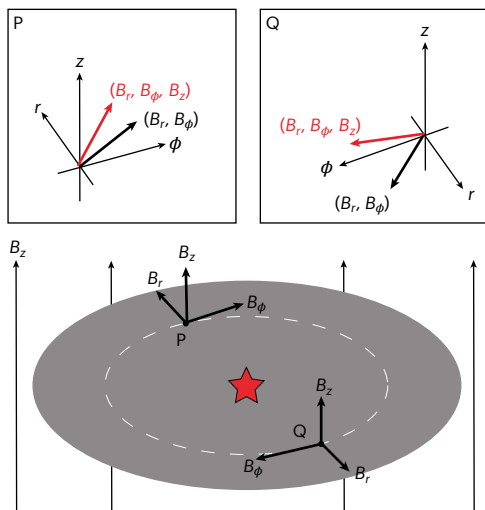


Fig. 4 | Schematic view of the three-dimensional magnetic field structure. We propose that the dependence of the angular offsets ($\Delta\phi$) on the disk position angle (shown in Fig. 3) is caused by the three-dimensional magnetic field structure of the disk as B_r , B_ϕ and B_z . At position P, the radial and vertical magnetic fields point in the same direction, strengthening the offset from the azimuthal direction, whereas at position Q, the radial and vertical magnetic fields point in opposite directions, weakening the offset from the azimuthal direction. Therefore, $\Delta\phi$ varies with the disk position angle.

dual-layer model. To confirm this, different magnetic field strengths are also plotted (coloured dashed lines in Fig. 6). We found that larger B_z causes a smaller angular offset of $\Delta\phi$ around the disk major axis (position angle of 150°) and a larger angular offset around the disk minor axis (position angle of 220°). This is because B_z has the same direction as B_ϕ along the disk major axis (which suppresses $\Delta\phi$) and as B_r along the disk minor axis (which enhances $\Delta\phi$). We also found that B_z becomes more efficient when it has the same direction as B_ϕ than when it has the opposite direction to B_ϕ in the dual-layer model because the projected length of the elongated dust grains becomes longer. By contrast, the previous single-layer model can enhance $\Delta\phi$ in the disk major axis and suppress $\Delta\phi$ in the disk minor axis by changing the direction of B_z with respect to B_r . Therefore, the best-fitting parameter of the single-layer model suggests that the B_r and B_z directions are opposite to each other. That is, if B_r is outward, then B_z is from south to north in the sky-projected direction.

These models imply that the single-layer model can reproduce the observed features of the systemic offset and the variation with position angle better than the dual-layer model. This suggests that, due to turbulence, the magnetic field across the disk midplane is not purely symmetric. Some magnetohydrodynamics simulations have shown such asymmetric magnetic field structures²⁹, although few simulations have been performed for disks with substructures such as rings and crescents³⁰. It is possible that the magnetic field in a crescent disk like this one is not a simple symmetric structure across the midplane. It will be necessary to investigate in further simulations the magnetic field in ring or crescent structures. Note that the emission was estimated to be optically thin ($\tau \approx 0.1$) in the southern region at a wavelength of 0.87 mm, suggesting that the polarized emission is the average value along the vertical direction of the scale height and mainly traces the midplane region. This also indicates that the single-layer model is better than the dual-layer model, because B_ϕ is assumed to fall at the disk midplane in the dual-layer model so that it can flip direction, whereas the observations indicate that B_ϕ is the dominant component of the disk magnetic field. Although different values of B_z were estimated by the two models, B_r has almost the same strength of $B_r \approx (0.2-0.3)B_\phi$ in both. This is because B_r was mainly determined by the systemic

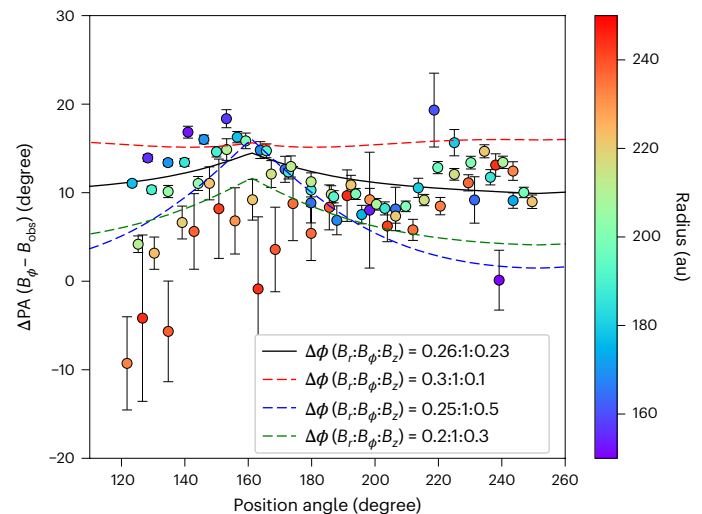


Fig. 5 | Angular offset for various relative magnetic field strengths. Angular difference ($\Delta\phi = B_\phi - B_{\text{obs}}$) between the observed magnetic field (B_{obs}) and the pure toroidal magnetic field (B_ϕ) as a function of position angle at 200 ± 50 au from the central star in the southern region. The colour indicates the radius from the central star. The data were obtained using Nyquist sampling (half of the beam size) with a disk radius of 200 ± 50 au. The data are presented as the median of the distribution with the errors corresponding to the 68th percentiles. There is a systemic offset of about 10° , which is caused by the contributions of the radial (B_r) and vertical (B_z) magnetic fields. The black line shows the best-fitting parameter $|B_r|:|B_\phi|:|B_z| = 0.26:1:0.23$ that explains this offset. The dashed coloured lines indicate the different relative magnetic field strengths, $|B_r|:|B_\phi|:|B_z| = 0.3:1:0.1$ (red), $0.25:1:0.5$ (blue) and $0.2:1:0.3$ (green), which shows the dependence of $\Delta\phi$ on the relative magnetic field strengths.

offset of $\Delta\phi$, whereas B_z was determined by the variation of $\Delta\phi$ with the position angle. Therefore, B_r could be estimated better than B_z , and $B_r \approx (0.2-0.3)B_\phi$ is robust. As the reduced chi-square values for both the single- and dual-layer models are much larger than 1 (9 for the single-layer model and 16 for the dual-layer model), more detailed observations and refined models are necessary to provide a better understanding of the fine magnetic structure, such as the radial distributions of B_r and B_z .

Magnetic field strength and activity

Our results for the relative magnetic field strength allowed us to estimate important physical parameters related to the disk magnetic field based on observations. To realize $B_z/B_\phi \approx 0.23$ in the disk around HD 142527, we estimated the ambipolar resistivity $\eta_A \approx 3.0 \times 10^{17} \text{ cm}^2 \text{ s}^{-1}$, the magnetic field strength $B \approx 0.3 \text{ mG}$, the ambipolar Elsasser number $\text{Am} \approx 0.4$ and the plasma beta $\beta \approx 2.0 \times 10^2$ (Methods). The Am parameter is a dimensionless number that characterizes the ambipolar diffusion. From these estimates, we suggest that magnetorotational instability can occur in the southern region of HD 142527, whereas Am and β are close to the boundary between active and inactive parameters for the magnetorotational instability³¹. This is consistent with near-infrared observations, which suggest that the HD 142527 disk is turbulent³². Furthermore, the magnetic field strength of 0.3 mG at ~ 200 au from the central star is consistent with a prediction from numerical simulations³³ and within the upper limit constrained by Zeeman observations³⁴. By assuming that B_z has a power-law profile $B_z \propto r^p$, the power-law index was estimated to be $p \approx -1$ from the relative strengths of B_r/B_z (Methods). Such a power-law profile of the vertical magnetic field suggests that the magnetic field increases moderately towards the centre. That the power exponent of the magnetic field is flatter than 2 suggests that the frozen magnetic flux has thawed and that both magnetic field advection and outward diffusion play a role^{35,36}.

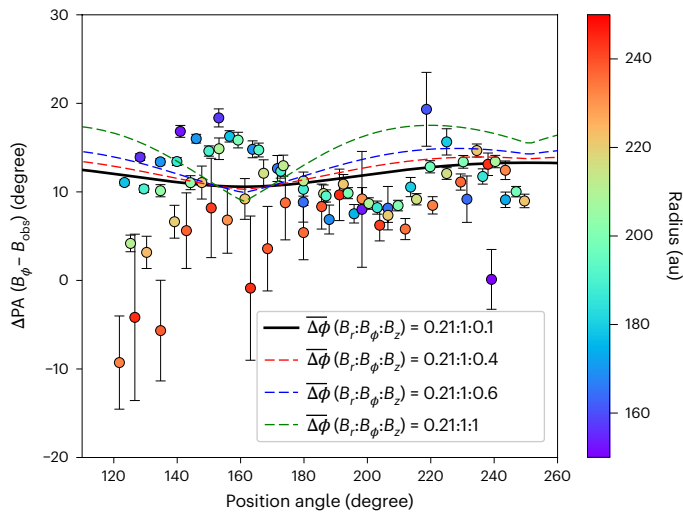


Fig. 6 | Angular differences for various relative magnetic field strengths in the dual-layer model. Angular difference ($\Delta\phi = B_\phi - B_{\text{obs}}$) between the observed magnetic field (B_{obs}) and the pure toroidal magnetic field (B_ϕ) as a function of position angle at 200 ± 50 au from the central star in the southern region. The colour indicates the radius from the central star. The data were obtained using Nyquist sampling (half of the beam size) with a disk radius of 200 ± 50 au. The data are presented as the median of the distribution with the errors corresponding to the 68th percentiles. There is a systemic offset of about 10° , which is caused by the contributions of the radial (B_r) and vertical (B_z) magnetic fields. For the dual-layer model of the magnetic field, the best fit gives $|B_r|:|B_\phi|:|B_z| \approx 0.21:1:0.1$, as shown by the black line. The different relative strengths are plotted as the coloured dashed lines: $|B_r|:|B_\phi|:|B_z| = 0.21:1:0.4$ (red), $0.21:1:0.6$ (blue) and $0.21:1:1$ (green).

The relative strengths of the three components of the magnetic field also have important implications for disk evolution processes^{25,26,37}. For example, angular momentum transport due to the magnetic field can be inferred from the Maxwell's stress M , as $M_{r\phi} = B_r B_\phi / 4\pi$ and $M_{z\phi} = B_z B_\phi / 4\pi$ along the radial (mass accretion) and vertical (disk wind) directions, respectively. The alpha value is commonly used to evaluate the angular momentum transport as $\alpha_{r\phi} = M_{r\phi} / \rho c_s^2 = 2B_r / \beta_\phi B_\phi$ and $\alpha_{z\phi} = M_{z\phi} / \rho c_s^2 = 2B_z / \beta_\phi B_\phi$. In our analysis, β was found to be $\sim 2.0 \times 10^2$. Therefore, the alpha values are $\alpha_{r\phi} \approx 0.53/\beta = 2.5 \times 10^{-3}$ and $\alpha_{z\phi} \approx 0.6/\beta = 2.2 \times 10^{-3}$, respectively. We, therefore, conclude that the angular momentum transports in the radial and vertical directions are comparable in the ~ 200 au region of the protoplanetary disk around HD 142527.

In this paper, we demonstrated that dust polarization can be used as a magnetic tracer for protoplanetary disks when the dust grains are as small as those in the interstellar medium. The three-dimensional magnetic field can be probed for a disk with moderate inclination. Our analyses allowed us to estimate several physical parameters related to the magnetic field in the disk and provide insights into angular momentum transfer, which is an important process determining the evolution of the disk. This method is also applicable to other disks. Thus, our observations shed light on the study of the magnetic field in protoplanetary disks.

Methods

Observations and data reduction

We used archival data from ALMA projects 2015.1.00425.S, 2017.1.00987.S, 2018.1.01172.S and 2022.1.00406.S for this study. The results of the projects 2015.1.00425.S and 2018.1.01172.S have been presented previously^{10,12,13}. These projects observed HD 142527 with full Stokes polarization. The basic parameters of these observations are summarized in Supplementary Table 1. The polarization calibrator was observed 3 or 4 times with ~ 6 min of integration time during each observing schedule to calibrate the instrumental polarization

(D-terms), cross-hand delay and cross-hand phase. The reduction and calibration of the data were performed in a standard manner using CASA³⁸.

Project 2015.1.00425.S was carried out on 11 March 2016 during its cycle 3 operation and on 21 May 2017 during its cycle 4 operation. The correlator set-up consisted of four spectral windows with a bandwidth of 1.75 GHz centred at sky frequencies of 336.5, 338.5, 348.5 and 350.5 GHz, providing a total bandwidth of ~ 7.5 GHz. The total integration times for the target were 73 min in cycle 3 operation and 80 min in cycle 4 operation.

Project 2017.1.00987.S was carried out on 7 January 2018 during its cycle 5 operation. The correlator set-up consisted of four 2 GHz spectral windows centred at sky frequencies of 137.995, 139.932, 149.995 and 151.995 GHz, providing a total bandwidth of ~ 8 GHz.

Project 2018.1.01172.S was carried out on 29 April 2019 during its cycle 6 operation. The correlator set-up consisted of four spectral windows. One band was set for 1.3 mm dust continuum emission centred at sky frequency 234.5 GHz with a bandwidth of 2 GHz. The other three windows had a bandwidth of 59 MHz and were centred on CO ($J=2 \rightarrow 1$), ^{13}CO ($J=2 \rightarrow 1$) and C^{18}O ($J=2 \rightarrow 1$) emission lines. In this paper, we used the spectral window of the 1.3 mm dust continuum emission.

Project 2022.1.00406.S was carried out on 26, 27, 30 and 31 March 2023 during its cycle 9 operation. The correlator set-up consisted of four spectral windows, and one band was set for 2.7 mm dust continuum emission centred at sky frequency 112 GHz with a bandwidth of 2 GHz. The other three windows had a bandwidth of 59 MHz and were centred on ^{13}CO ($J=1 \rightarrow 0$), C^{18}O ($J=1 \rightarrow 0$) and CN ($N=1 \rightarrow 0$, $J=1/2 \rightarrow 1/2$ and $F=1/2 \rightarrow 1/2$) emission lines. In this paper, we used the spectral window of the 2.7 mm dust continuum emission.

Imaging

Stokes I , Q and U images were generated from the calibrated visibility data by the CASA task tclean. To improve image fidelity, we performed an iterative phase-only self-calibration using the initial clean image as the first model image in CASA 6.5.1 for all projects except 2022.1.00406.S, as it was not improved by self-calibration. The time needed to solve the complex gain was reduced from infinity to 300 s and finally to 60 s. All images were generated with Briggs weighting. The robust parameters and the resulting parameters for the images are summarized in Supplementary Table 2. The PI was calculated from Stokes Q and U and has a positive bias because the Stokes Q and U components give the polarized intensity as $\sqrt{Q^2 + U^2}$. This bias is particularly noticeable in low signal-to-noise measurements. We, therefore, debiased the PI image as $\text{PI} = \sqrt{Q^2 + U^2 - \sigma_{\text{PI}}^2}$, where σ_{PI} is the root-mean-square noise level^{39,40}. The PF image was generated by $\text{PF}(\%) = \text{PI} / (\text{Stokes } I) \times 100$ when the PI emission was above the noise level $3\sigma_{\text{PI}}$. The polarization vectors were calculated from Stokes Q and U as $\text{PA} = \frac{1}{2} \arctan \left(\frac{\text{Stokes } U}{\text{Stokes } Q} \right)$ when the PI emission was above the $3\sigma_{\text{PI}}$ noise level.

Imaging the differences between polarization vectors and polarization fractions

To avoid confounding by different spatial frequency components, the images of the polarization vector differences (Supplementary Fig. 1) were generated using the same uv distance. Note that uv is defined as the projected length of the baseline vector between two antennas in the Fourier (uv) plane. The uv distance is given by $\sqrt{u^2 + v^2}$, and it corresponds to the spatial frequency sampled by the interferometer. For $\Delta\text{PA}_{1.3\text{mm}-0.87\text{mm}} = \text{PA}_{1.3\text{mm}} - \text{PA}_{0.87\text{mm}}$, the Stokes Q and U images for the 0.87 and 1.3 mm polarization data were generated using uv distances of $1.4 \times 10^4 \lambda$ to $5.5 \times 10^5 \lambda$. The Stokes Q and U images for the 0.87 mm data were smoothed to a beam size of $0.517'' \times 0.452''$ with a position angle of 64.2° to match the 1.3 mm data. The polarization vectors were then calculated from the Stokes Q and U images when the PI emission was above the 3σ levels. The σ_{PI} was derived to be 35 and 23 μJy per beam for 0.87 and 1.3 mm, respectively.

For $\Delta PA_{2.1\text{mm}-0.87\text{mm}} = PA_{2.1\text{mm}} - PA_{0.87\text{mm}}$, the Stokes Q and U images for the 0.87 and 1.3 mm polarization data were generated using a uv distance of $1.4 \times 10^4 \lambda$ to $1.2 \times 10^6 \lambda$. The Stokes Q and U images for the 0.87 mm data were smoothed to a beam size of $0.479'' \times 0.405''$ with a position angle of 76.1° to match the 2.1 mm data. Then, the polarization vectors were calculated from the Stokes Q and U images. The polarization vectors were calculated when the PI emission was above the 3σ levels, where σ_{PI} was derived to be 33 and 7.6 μJy per beam at 0.87 and 2.1 mm, respectively. To make the images of the ratios of the polarization fractions (Supplementary Fig. 3), the polarization fractions were also calculated by the above method. The polarization fractions were calculated when the PI emission was above the 3σ levels.

For $\Delta PA_{2.7\text{mm}-0.87\text{mm}} = PA_{2.7\text{mm}} - PA_{0.87\text{mm}}$, the Stokes Q and U images for the 0.87 and 2.7 mm polarization data were generated using a uv distance of $1.4 \times 10^4 \lambda$ to $4.7 \times 10^5 \lambda$. The Stokes Q and U images for the 0.87 mm data were smoothed to a beam size of $0.711'' \times 0.678''$ with a position angle of 50.6° to match the 2.7 mm data. Then, the polarization vectors were calculated from the Stokes Q and U images. The polarization vectors were calculated when the PI emission was above the 3σ levels, where σ_{PI} was derived to be 54 and 7.4 μJy per beam at 0.87 and 2.7 mm, respectively. To make the images of the ratios of the polarization fractions (Supplementary Fig. 3), the polarization fractions were also calculated with the above method. The polarization fractions were calculated when the PI emission was above the 3σ levels.

To evaluate the wavelength dependence of the polarization patterns, we calculated the differences for the polarization vectors at 1.3, 2.1 and 2.7 mm with respect to the 0.87 mm polarization vectors by deriving $\Delta PA_{1.3\text{mm}-0.87\text{mm}} = PA_{1.3\text{mm}} - PA_{0.87\text{mm}}$, $\Delta PA_{2.1\text{mm}-0.87\text{mm}} = PA_{2.1\text{mm}} - PA_{0.87\text{mm}}$ and $\Delta PA_{2.7\text{mm}-0.87\text{mm}} = PA_{2.7\text{mm}} - PA_{0.87\text{mm}}$. Supplementary Fig. 1 shows the differences in the polarization vectors. In the northern region, $\Delta PA_{1.3\text{mm}-0.87\text{mm}}$, $\Delta PA_{2.1\text{mm}-0.87\text{mm}}$ and $\Delta PA_{2.7\text{mm}-0.87\text{mm}}$ are all $\sim 90^\circ$ on the ridge of the horseshoe structure, indicating that $PA_{0.87\text{mm}}$ is perpendicular to $PA_{1.3\text{mm}}$, $PA_{2.1\text{mm}}$ and $PA_{2.7\text{mm}}$. By contrast, in the southern region, the polarization vectors are almost in the same direction ($\Delta PA_{1.3\text{mm}-0.87\text{mm}}$, $\Delta PA_{2.1\text{mm}-0.87\text{mm}}$ and $\Delta PA_{2.7\text{mm}-0.87\text{mm}} \approx 0^\circ$). Supplementary Fig. 2 plots $\Delta PA_{1.3\text{mm}-0.87\text{mm}}$, $\Delta PA_{2.1\text{mm}-0.87\text{mm}}$ and $\Delta PA_{2.7\text{mm}-0.87\text{mm}}$ as functions of position angles of $110\text{--}250^\circ$ on the ridge of the southern part of the horseshoe structure. The plotted data were taken from the pixels at the ridge position with a Nyquist sampling of 11° for $\Delta PA_{1.3\text{mm}-0.87\text{mm}}$, 10° for $\Delta PA_{2.1\text{mm}-0.87\text{mm}}$ and 15° for $\Delta PA_{2.7\text{mm}-0.87\text{mm}}$. The differences for the polarization vectors were derived to be $\Delta PA_{1.3\text{mm}-0.87\text{mm}} = 3.9 \pm 0.6^\circ$, $\Delta PA_{2.1\text{mm}-0.87\text{mm}} = 1 \pm 1^\circ$ and $\Delta PA_{2.7\text{mm}-0.87\text{mm}} = -5.2 \pm 3.4^\circ$. Supplementary Figs. 1 and 2 show that the polarization vectors have almost the same directions across all the wavelengths. Although larger angular offsets are seen at longer wavelength separations, this may be due to the weaker emission at longer wavelengths. The 2.7 mm polarization emission in band 3 is the weakest emission with the largest beam size, leading to larger uncertainties in the polarization vectors due to the noise. In addition to the polarization vectors, Supplementary Fig. 3 shows the ratios of the polarization fraction $P_{\text{frac},1.3\text{mm}}/P_{\text{frac},0.87\text{mm}}$, $P_{\text{frac},2.1\text{mm}}/P_{\text{frac},0.87\text{mm}}$ and $P_{\text{frac},2.7\text{mm}}/P_{\text{frac},0.87\text{mm}}$ (Methods). In the northern region, the polarization fractions differ significantly, with $P_{\text{frac},1.3\text{mm}}/P_{\text{frac},0.87\text{mm}}$ reaching values as high as ~ 5 and $P_{\text{frac},2.1\text{mm}}/P_{\text{frac},0.87\text{mm}}$ and $P_{\text{frac},2.7\text{mm}}/P_{\text{frac},0.87\text{mm}}$ reaching values as high as ~ 10 . By contrast, in the southern region, the polarization fractions are almost the same values, as all the polarization fraction ratios are ~ 1 .

The dual-layer model for the angular offset

In Fig. 3, we have considered the single-layer magnetic field to estimate the relative strengths. However, B_ϕ and B_r were assumed to be in opposite directions in the upper and lower disk layers because these magnetic fields are generated by the entrainment and accretion of the initial B_z due to the rotation (Extended Data Fig. 1). Thus, the observed offset may be due to a combination of the upper disk layer ($\Delta\phi_+$) and the lower disk layer ($\Delta\phi_-$).

By assuming that the radial and toroidal magnetic fields in the lower layer have the same strengths but in opposite directions to those in the upper layer, the angular offset of the lower layer ($\Delta\phi_-$) was estimated as $\Delta\phi_- = \arctan \frac{-(B_r)_\phi + (B_z)_{\text{proj}}}{-(B_r)_\phi + (B_z)_{\text{proj}}}$. Because the 0.87 mm dust continuum emission is optically thin ($\tau < 0.1$), the angular offset ($\Delta\phi$) should be the weighted average of $\Delta\phi_+$ and $\Delta\phi_-$:

$$\overline{\Delta\phi} = \frac{1}{2} \arctan \frac{\text{Stokes } U_{\Delta\phi_+} + \text{Stokes } U_{\Delta\phi_-}}{\text{Stokes } Q_{\Delta\phi_+} + \text{Stokes } Q_{\Delta\phi_-}}, \quad (2)$$

where the subscripts $\Delta\phi_+$ and $\Delta\phi_-$ in the Stokes Q and Stokes U parameters represent emission from the upper and lower layers, respectively. The $\overline{\Delta\phi}$ value is not simply determined by the combination of $\Delta\phi_+$ and $\Delta\phi_-$ but by the combination of the Stokes Q and U emission.

The polarization fraction was calculated with $p \approx p_{\text{max}} \sin^2 \theta$, where θ is the projected length of the elongated dust grains along the plane of the sky^{41,42} and p_{max} is defined as the intrinsic polarization, which is the maximum polarization when the grains are perfectly aligned in the same direction. However, p_{max} can be ignored in this calculation because we assume the same p_{max} between the upper and lower layers. Then, the $\overline{\Delta\phi}$ value is independent of p_{max} . Therefore, Stokes Q and Stokes U were derived only from $\sin^2 \theta$ in both layers.

Estimating the magnetic field strength and power-law of the vertical magnetic field

From the relative strengths of the three-dimensional magnetic fields, we estimated the magnetic field strength and the power-law profile of the vertical magnetic field with radius. By assuming a balance between the generation of B_ϕ by vertical shear motion and the dissipation of B_ϕ by ambipolar diffusion, B_ϕ can be estimated⁴³ as

$$B_\phi = \left(\frac{H}{r}\right)^2 \left(\frac{B_z H}{\eta_A}\right) v_\phi = \frac{H^3}{r} \frac{\Omega_K}{\eta_A} B_z, \quad (3)$$

where H , r , η_A , v_ϕ and Ω_K are the gas scale height, radius, ambipolar resistivity, Kepler velocity and Kepler frequency. Therefore, the ambipolar resistivity can be written as $\eta_A = \frac{H^3 \Omega_K}{c_s} \frac{B_z}{B_\phi}$. The gas scale height is given by $H = c_s / \Omega_K$, where c_s is the speed of sound. Here we assumed that the dust scale height is the same as the gas scale height because it has been suggested that this disk is highly turbulent³². The turbulent strength (α) and dust size (a_{dust}) were estimated to be $\alpha \approx 0.3$ and $a_{\text{dust}} \approx 3 \mu\text{m}$, respectively, from near-infrared observations with the compact dust assumption. Then, the dust scale height can be calculated

as $H_{\text{dust}} = \left(1 + \frac{\text{St}}{\alpha} \frac{1+2\text{St}}{1+\text{St}}\right)^{-1/2} H_{\text{gas}}$ (refs. 44,45), where $\text{St} = (\pi \rho a_{\text{dust}}) / (2 \Sigma_{\text{gas}})$ is

the Stokes number estimated from the dust internal density (ρ), dust size (a_{dust}), and gas surface density (Σ_{gas}). Therefore, $H_{\text{dust}} \approx H_{\text{gas}}$ when the dust size is less than $100 \mu\text{m}$, assuming a gas surface density of 0.2 g cm^{-2} and a turbulent strength $\alpha = 0.3$. Note that the turbulent strength has been studied for different porous dust grains and dust surface densities by keeping a fixed value of St/α (ref. 32). Even if the dust structure and dust surface density are changed, our assumption of $H_{\text{dust}} \approx H_{\text{gas}}$ is robust as long as St/α does not change. In addition, we assumed that the relative strengths of the magnetic field do not vary much within the dust scale height. This is suggested to be a reasonable assumption for B_z , because the variation of B_z within the gas scale height is estimated to be $\Delta B_z \approx (H/r) B_r \approx (Hr) / B_z$ (ref. 46). Here, $r \approx 200 \text{ au}$ and $H \approx 20 \text{ au}$. Therefore, ΔB_z can be negligible. By contrast, the variations of B_r and B_ϕ within the gas scale height are unknown parameters and have been studied by magnetohydrodynamics simulations. If the single-layer model applies, it can be speculated that the strengths of B_r and B_ϕ do not vary as much within the scale height²⁹. In the dual-layer model, the polarized emission is from the relatively upper layer because B_ϕ will fall at the disk midplane so that its direction can reverse, whereas

the observations indicate that B_ϕ is the dominant component. Note that the emission was estimated to be optically thin ($\tau \approx 0.1$) at a wavelength of 0.87 mm, suggesting that the polarized emission is the average value along the vertical direction of the scale height and could mainly trace the midplane region. This also indicates that the single-layer model is better than the dual-layer model.

By considering a central star of mass $2.4 M_\odot$, temperature 30 K and $B_z/B_\phi = 0.23$, η_A was derived to be $2.3 \times 10^{17} \text{ cm}^2 \text{ s}^{-1}$. Then, because the gas density was small enough, the ambipolar resistivity was approximated as $\eta_A = B^2/(4\pi C\gamma\rho^{3/2})$ (refs. 43,47). Here $C = \sqrt{n_i^2\zeta_{\text{CR}}/m_g\beta_r}$, where m_i and m_g are the masses of ions and neutral particles. We adopted $m_i = 29m_{\text{H}}$ and $m_g = 2.34m_{\text{H}}$ assuming that the major ion is HCO^+ , where m_{H} is the hydrogen mass. The HCO^+ molecule has been suggested to be the most abundant ion when the abundance ratio of $n(\text{CO})/n(\text{electron})$ is higher than $\sim 10^3$ (ref. 48). Although the electron abundance is not well constrained, it is usually assumed to be $X(e) \lesssim 10^{-9}$. On the other hand, the CO abundance has been estimated to be $X(\text{CO}) \approx 10^{-4}$ for the HD 142527 disk¹¹. Therefore, we assumed that the HCO^+ molecule is the most abundant ion for this region. ζ_{CR} is the cosmic ray ionization rate, which we assumed was 10^{-17} s^{-1} . β_r is the recombination rate and was assumed to be $\beta_r = \beta_{r,0}(T/300 \text{ K})^{-0.67}$, where $\beta_{r,0} = 2.4 \times 10^{-7} \text{ cm}^3 \text{ s}^{-1}$.

$\gamma = \langle\sigma v\rangle_{\text{in}}/(m_g + m_i)$ where $\langle\sigma v\rangle_{\text{in}}$ is the rate coefficient for collisional momentum transfer between ions and neutrals. We assumed $\langle\sigma v\rangle_{\text{in}} = 1.3 \times 10^{-9} \text{ cm}^3 \text{ s}^{-1}$. We estimated the magnetic field strength with this formula. The gas density ρ was derived to be $\rho = \Sigma_g/H$, where Σ_g is the gas surface density, which was derived to be $\Sigma_g = 0.2 \text{ g cm}^{-2}$ (ref. 11). From these parameters, the magnetic field strength was finally derived to be $B \approx 0.3 \text{ mG}$. The Am parameter was also estimated from the magnetic field strength. The Am parameter is defined as $\text{Am} = v_A^2/\eta_A\Omega_K = B^2/(\eta_A\Omega_K \times 4\pi\rho)$, where v_A is the Alfvén velocity, $v_A = \sqrt{B^2/4\pi\rho}$. By assuming $B \approx 0.3 \text{ mG}$, $\eta_A = 2.3 \times 10^{17} \text{ cm}^2 \text{ s}^{-1}$ and $\rho = 6.6 \times 10^{-16} \text{ g cm}^{-3}$, the Am parameter was derived to be $\text{Am} \approx 0.4$. The plasma beta is defined as $\beta = 8\pi\rho c_s^2/B^2$ and was derived to be $\beta \approx 2.0 \times 10^2$.

By assuming that B_z has a power-law profile $B_z \propto r^p$, the power-law index p was estimated from the relative strengths between B_r and B_z . The radial magnetic field B_r was obtained approximately as $B_r = \Psi(r)/2\pi r^2$, where $\Psi(r)$ is the magnetic flux enclosed within a radius r and is given by $\Psi = \int_0^r 2\pi r B_z dr$. By assuming the power-law profile $B_z = B_{z,0}(r/1 \text{ au})^p$, $\Psi(r) = \int_0^r 2\pi r B_{z,0} \left(\frac{r}{1 \text{ au}}\right)^p dr = \frac{2\pi B_{z,0}}{p+2} \left(\frac{r}{1 \text{ au}}\right)^{p+2}$, where $B_{z,0}$ is the vertical magnetic field strength at a radius of 1 au. From the magnetic flux, B_r can be written as $B_r = \frac{2\pi B_{z,0}}{p+2} \left(\frac{r}{1 \text{ au}}\right)^{p+2} \frac{1}{2\pi r^2} = \frac{B_{z,0}}{(p+2)} \left(\frac{r}{1 \text{ au}}\right)^p$. Therefore, $\frac{B_r}{B_z} = \frac{1}{(p+2)}$. As $\frac{|B_r|}{|B_z|} \approx 1$ around a radius of 200 au, the power-law index was derived to be $p \approx -1$. This implies that the magnetic field increases moderately towards the centre. That the power exponent of the magnetic field is flatter than 2 suggests that the frozen magnetic flux has thawed and that both magnetic field advection and outward diffusion both play a role^{35,36}.

Data availability

The datasets generated and analysed during the current study are available in the ALMA archive, <https://almascience.nrao.edu/alma-data/archive>, with programme IDs 2015.1.00425.S, 2017.1.00987.S, 2018.1.01172.S and 2022.1.00406.S.

Code availability

The Python packages used in the data analysis are all publicly available. The calibration and chi-square fitting scripts are available from the corresponding author upon reasonable request.

References

- Waelkens, C. et al. SWS observations of young main-sequence stars with dusty circumstellar disks. *Astron. Astrophys.* **315**, L245–L248 (1996).
- Arun, R. et al. On the mass accretion rate and infrared excess in Herbig Ae/Be stars. *Astron. J.* **157**, 159 (2019).
- Fukagawa, M. et al. Near-infrared images of protoplanetary disk surrounding HD 142527. *Astrophys. J. Lett.* **636**, L153–L156 (2006).
- Verhoeff, A. P. et al. The complex circumstellar environment of HD 142527. *Astron. Astrophys.* **528**, A91 (2011).
- Gaia Collaboration. Gaia Data Release 1. Summary of the astrometric, photometric, and survey properties. *Astron. Astrophys.* **595**, A2 (2016).
- Gaia Collaboration. The Gaia mission. *Astron. Astrophys.* **595**, A1 (2016).
- Mendigutía, I. et al. Stellar parameters and accretion rate of the transition disk star HD 142527 from X-Shooter. *Astrophys. J.* **790**, 21 (2014).
- Casassus, S. et al. Flows of gas through a protoplanetary gap. *Nature* **493**, 191–194 (2013).
- Fukagawa, M. et al. Local enhancement of the surface density in the protoplanetary ring surrounding HD 142527. *Publ. Astron. Soc. Jpn* **65**, L14 (2013).
- Ohashi, S. et al. Two different grain size distributions within the protoplanetary disk around HD 142527 revealed by ALMA polarization observation. *Astrophys. J.* **864**, 81 (2018).
- Soon, K.-L. et al. Investigating the gas-to-dust ratio in the protoplanetary disk of HD 142527. *Publ. Astron. Soc. Jpn* **71**, 124 (2019).
- Kataoka, A. et al. Submillimeter polarization observation of the protoplanetary disk around HD 142527. *Astrophys. J. Lett.* **831**, L12 (2016).
- Stephens, I. W., Fernández-López, M., Li, Z.-Y., Looney, L. W. & Teague, R. Low-level carbon monoxide line polarization in two protoplanetary disks: HD 142527 and IM Lup. *Astrophys. J.* **901**, 71 (2020).
- Kataoka, A. et al. Millimeter-wave polarization of protoplanetary disks due to dust scattering. *Astrophys. J.* **809**, 78 (2015).
- Lazarian, A. & Hoang, T. Radiative torques: analytical model and basic properties. *Mon. Not. R. Astron. Soc.* **378**, 910–946 (2007).
- Andersson, B. G., Lazarian, A. & Vaillancourt, J. E. Interstellar dust grain alignment. *Annu. Rev. Astron. Astrophys.* **53**, 501–539 (2015).
- Hoang, T. et al. On internal and external alignment of dust grains in protostellar environments. *Astron. J.* **164**, 248 (2022).
- Cho, J. & Lazarian, A. Grain alignment and polarized emission from magnetized T Tauri disks. *Astrophys. J.* **669**, 1085–1097 (2007).
- Bertrang, G. H. M., Flock, M. & Wolf, S. Magnetic fields in protoplanetary discs: from MHD simulations to ALMA observations. *Mon. Not. R. Astron. Soc.* **464**, L61–L64 (2017).
- Tazaki, R., Lazarian, A. & Nomura, H. Radiative grain alignment in protoplanetary disks: implications for polarimetric observations. *Astrophys. J.* **839**, 56 (2017).
- Kataoka, A., Okuzumi, S. & Tazaki, R. Millimeter-wave polarization due to grain alignment by the gas flow in protoplanetary disks. *Astrophys. J. Lett.* **874**, L6 (2019).
- Yang, H., Li, Z.-Y., Stephens, I. W., Kataoka, A. & Looney, L. Does HL Tau disc polarization in ALMA band 3 come from radiatively aligned grains? *Mon. Not. R. Astron. Soc.* **483**, 2371–2381 (2019).
- Guillet, V., Girart, J. M., Maury, A. J. & Alves, F. O. Polarized emission by aligned grains in the Mie regime: application to protoplanetary disks observed by ALMA. *Astron. Astrophys.* **634**, L15 (2020).
- Hoang, T., Cho, J. & Lazarian, A. Alignment of irregular grains by mechanical torques. *Astrophys. J.* **852**, 129 (2018).
- Wardle, M. Magnetic fields in protoplanetary disks. *Astrophys. Space Sci.* **311**, 35–45 (2007).
- Bai, X.-N. & Stone, J. M. Wind-driven accretion in protoplanetary disks. I. Suppression of the magnetorotational instability and launching of the magnetocentrifugal wind. *Astrophys. J.* **769**, 76 (2013).

27. Suzuki, T. K. & Inutsuka, S.-i. Magnetohydrodynamic simulations of global accretion disks with vertical magnetic fields. *Astrophys. J.* **784**, 121 (2014).
28. Boehler, Y. et al. Vortex-like kinematic signal, spirals, and beam smearing effect in the HD 142527 disk. *Astron. Astrophys.* **650**, A59 (2021).
29. Bai, X.-N. Global simulations of the inner regions of protoplanetary disks with comprehensive disk microphysics. *Astrophys. J.* **845**, 75 (2017).
30. Suriano, S. S., Li, Z.-Y., Krasnopolsky, R. & Shang, H. The formation of rings and gaps in magnetically coupled disc-wind systems: ambipolar diffusion and reconnection. *Mon. Not. R. Astron. Soc.* **477**, 1239–1257 (2018).
31. Bai, X.-N. & Stone, J. M. Effect of ambipolar diffusion on the nonlinear evolution of magnetorotational instability in weakly ionized disks. *Astrophys. J.* **736**, 144 (2011).
32. Tazaki, R., Murakawa, K., Muto, T., Honda, M. & Inoue, A. K. The water-ice feature in near-infrared disk-scattered light around HD 142527: micron-sized icy grains lifted up to the disk surface? *Astrophys. J.* **921**, 173 (2021).
33. Bai, X.-N. Hall effect controlled gas dynamics in protoplanetary disks. II. Full 3D simulations toward the outer disk. *Astrophys. J.* **798**, 84 (2015).
34. Vlemmings, W. H. T. et al. Stringent limits on the magnetic field strength in the disc of TW Hya. ALMA observations of CN polarisation. *Astron. Astrophys.* **624**, L7 (2019).
35. Guilet, J. & Ogilvie, G. I. Global evolution of the magnetic field in a thin disc and its consequences for protoplanetary systems. *Mon. Not. R. Astron. Soc.* **441**, 852–868 (2014).
36. Tsukamoto, Y. Co-evolution of dust grains and protoplanetary disks. II. Structure and evolution of protoplanetary disks: an analytical approach. *Publ. Astron. Soc. Jpn* **76**, 674–687 (2024).
37. Hartmann, L., Herczeg, G. & Calvet, N. Accretion onto pre-main-sequence stars. *Annu. Rev. Astron. Astrophys.* **54**, 135–180 (2016).
38. McMullin, J. P., Waters, B., Schiebel, D., Young, W. & Golap, K. in *CASA Architecture and Applications*, Vol. 376 (eds Shaw, R. A. et al.) 127–130 (ASP, 2007).
39. Vaillancourt, J. E. Placing confidence limits on polarization measurements. *Publ. Astron. Soc. Pac.* **118**, 1340–1343 (2006).
40. Hull, C. L. H. & Plambeck, R. L. The 1.3 mm full-Stokes polarization system at CARMA. *J. Astron. Instrum.* **4**, 1550005 (2015).
41. Lee, H. M. & Draine, B. T. Infrared extinction and polarization due to partially aligned spheroidal grains: models for the dust toward the BN object. *Astrophys. J.* **290**, 211–228 (1985).
42. Yang, H. et al. Disc polarization from both emission and scattering of magnetically aligned grains: the case of NGC 1333 IRAS 4A1. *Mon. Not. R. Astron. Soc.* **460**, 4109–4121 (2016).
43. Tsukamoto, Y., Machida, M. N. & Inutsuka, S.-i. Co-evolution of dust grains and protoplanetary disks. *Publ. Astron. Soc. Jpn* **75**, 835–852 (2023).
44. Dubrulle, B., Morfill, G. & Sterzik, M. The dust subdisk in the protoplanetary nebula. *Icarus* **114**, 237–246 (1995).
45. Youdin, A. N. & Lithwick, Y. Particle stirring in turbulent gas disks: including orbital oscillations. *Icarus* **192**, 588–604 (2007).
46. Braiding, C. R. *Star Formation and the Hall Effect*. PhD thesis, Macquarie Univ. (2011).
47. Tsukamoto, Y. & Machida, M. N. Classification of the circumstellar disc evolution during the main accretion phase. *Mon. Not. R. Astron. Soc.* **416**, 591–600 (2011).
48. Aikawa, Y., Furuya, K., Nomura, H. & Qi, C. Analytical formulae of molecular ion abundances and the N₂H⁺ ring in protoplanetary disks. *Astrophys. J.* **807**, 120 (2015).

Acknowledgements

This paper makes use of the following ALMA data: ADS/JAO. ALMA#2015.1.00425.S, #2017.1.00987.S, #2018.1.01172.S and #2022.1.00406.S. ALMA is a partnership of ESO (representing its member states), NSF (USA) and NINS (Japan), together with NRC (Canada) and NSC and ASIAA (Taiwan) and KASI (Republic of Korea), in cooperation with the Republic of Chile. The Joint ALMA Observatory is operated by ESO, AUI/NRAO and NAOJ. S.O. acknowledges support from JSPS (KAKENHI Grant Nos. JP20K14533, JP22H01275 and JP23K22546). T.M. acknowledges support from JSPS (KAKENHI Grant No. JP23K03463). T.T. acknowledges support from JSPS (KAKENHI Grant Nos. JP20K04017 and JP24K07097). N.S. acknowledges support from JSPS (KAKENHI Grant No. JP20H00182).

Author contributions

This project was led by S.O., who was responsible for the analysis and wrote the paper together with T.M., Y.T. and M.M. Y.T. calculated the physical parameters, including the magnetic field strength from the relative strengths of the magnetic field. All authors contributed to the data analysis, discussed the results and contributed to the paper.

Competing interests

The authors declare no competing interests.

Additional information

Extended data is available for this paper at <https://doi.org/10.1038/s41550-024-02454-x>.

Supplementary information The online version contains supplementary material available at <https://doi.org/10.1038/s41550-024-02454-x>.

Correspondence and requests for materials should be addressed to Satoshi Ohashi.

Peer review information *Nature Astronomy* thanks Josep Girart and the other, anonymous, reviewer(s) for their contribution to the peer review of this work.

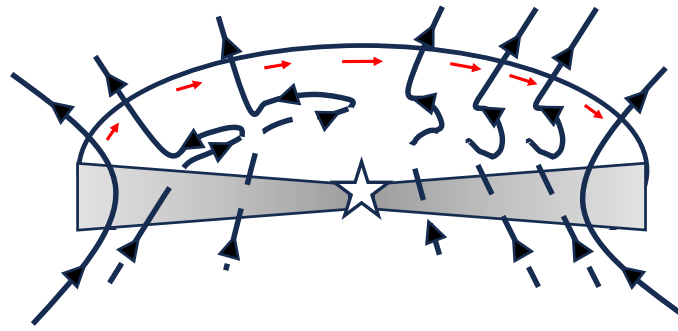
Reprints and permissions information is available at www.nature.com/reprints.

Publisher's note Springer Nature remains neutral with regard to jurisdictional claims in published maps and institutional affiliations.

Open Access This article is licensed under a Creative Commons Attribution-NonCommercial-NoDerivatives 4.0 International License, which permits any non-commercial use, sharing, distribution and reproduction in any medium or format, as long as you give appropriate credit to the original author(s) and the source, provide a link to the Creative Commons licence, and indicate if you modified the licensed material. You do not have permission under this licence to share adapted material derived from this article or parts of it. The images or other third party material in this article are included in the article's Creative Commons licence, unless indicated otherwise in a credit line to the material. If material is not included in the article's Creative Commons licence and your intended use is not permitted by statutory regulation or exceeds the permitted use, you will need to obtain permission directly from the copyright holder. To view a copy of this licence, visit <http://creativecommons.org/licenses/by-nc-nd/4.0/>.

© The Author(s) 2025

¹ALMA Project, National Astronomical Observatory of Japan, Tokyo, Japan. ²Cluster for Pioneering Research, RIKEN, Wako-shi, Japan. ³Division of Liberal Arts, Kogakuin University, Tokyo, Japan. ⁴Graduate Schools of Science and Engineering, Kagoshima University, Kagoshima, Japan. ⁵Department of Astronomical Science, University for Advanced Studies (SOKENDAI), Tokyo, Japan. ⁶Faculty of Engineering, Ashikaga University, Ashikaga, Japan. ⁷College of Science, Ibaraki University, Mito, Japan. ✉e-mail: satoshi.ohashi@nao.ac.jp



Extended Data Fig. 1 | A schematic view of the 3D configuration of the magnetic field in a protoplanetary disk. The black lines show the magnetic field, and the red arrows indicate the rotation direction. B_ϕ and B_r are generated

by the rotation of the initial state, B_z . Then, B_ϕ and B_r are likely to be in opposite directions with respect to the disk midplane due to the entrainment of the initial B_z field by the disk rotation.